Polarization structure of nanostrip domain intersections in GeTe films

Boris Croes,[1,2] Fabien Cheynis,[1] Salia Cherifi-Hertel,[2] Kokou Dodzi Dorkenoo,[2] Pierre Müller,[1] Stefano Curiotto,[1] and Frédéric Leroy[1,*]

[1]*Aix Marseille Univ, CNRS, CINAM, AMUTECH, Marseille, France*

[2]*Université de Strasbourg, CNRS, Institut de Physique et Chimie des Matériaux de Strasbourg, Strasbourg 67000, France*

(Received 12 September 2023; revised 7 December 2023; accepted 3 January 2024; published 16 January 2024)

Ferroelectric germanium telluride is under active consideration for spintronic and thermoelectric applications. The control of the ferroelectric domain walls is a key issue to optimize the electronic and thermal properties of GeTe thin films. Domain walls properties are usually driven by the mechanical and electrostatic compatibility conditions of twin domains. However, in dense ferroelectric domain structures these compatibility conditions are hardly fulfilled everywhere. In particular intersection of domains may result in complex lattice relaxations and polarization textures. In this study, we have fabricated GeTe thin films on silicon substrate and elucidated the intersections of *a*-type domains using 3D reciprocal space maps, scanning tunneling microscopy, and second-harmonic microscopy. We demonstrate the presence of complex structural reorganizations that manifest by the formation of charged domain walls, large lattice rotations, and enhanced stretching of the rhombohedral lattice.

DOI: 10.1103/PhysRevB.109.024103

I. INTRODUCTION

Ferroelectric thin films are the object of intense fundamental research stimulated by their applications as functional materials. The ability to synthesize ferroelectric thin films of high crystalline quality based on layer-by-layer growth techniques and strain engineering has made possible to discover novel phenomena based on the interplay between the stress induced by the substrate and the electrostatic boundary conditions. It has been demonstrated that flux-closure polar domains [1–3], vortices [4,5], and even skyrmions [6] could be obtained in ferroelectric materials. These novel structures can potentially exhibit enhanced electric conduction as measured at vortex cores in $BiFeO_3$ [2], high thermal resistance [7], or high Seebeck coefficient at charged domain walls [8]. Such properties could be used in future devices if the local ferroelectric polarization can be controlled. In the quest of enhanced ferroelectric properties, intersections of domain walls are expected to show highly polarized regions with complex polarization textures resulting from a strong relaxation of the lattice. Among ferroelectrics, GeTe has witnessed a sustained boom [9–14]. As a thermoelectrics, it has recently been demonstrated a record figure of merit ($zT \sim 2.4$) at 330°C for the ferroelectric GeTe phase [15]. In the meantime, major results have been obtained on ferroelectric GeTe thin films in the context of spintronic properties based on the Rashba effect [16]. It has been demonstrated the reversal of the ferroelectric polarization under an electric field [17] and a consistent change of the spin chirality of the band structure [18,19]. Even more fascinating GeTe thin films show remarkable transport properties at room temperature such as nonreciprocal charge transport [20] or ferroelectric switching of the spin-to-charge conversion [21].

All these results take advantage of the ferroelectric property of α-GeTe. This phase has a rhombohedral structure (space group R3m) and bulk Curie temperature well above room temperature ($T_c \sim 650 - 700$ K). The spontaneous polarization of α-GeTe is along the pseudocubic $\langle 111 \rangle_c$ leading to the formation of four ferroelastic variants (c stands for pseudocubic coordinates, see Supplemental Material [22]). As reported by Wang *et al.* [23] α-GeTe thin films can be grown with a quasisingle crystalline quality on Si(111) by molecular beam epitaxy using a predeposition of one monolayer of Sb onto the substrate. Despite a significant lattice mismatch of ~8.5% with the substrate, the GeTe layer is relaxed since the very beginning of growth. Croes *et al.* [24] have shown that GeTe thin films thicker than 30 nm have a multiple domain structure with all four ferroelastic variants. The main domain has a ferroelectric polarization perpendicular to the surface, i.e., in the $[111]_c$ direction, and is called c domain. The three other ferroelectric domains are called hereafter a domains and form 71°-type domain walls with the c domain. These domain walls ensure mechanical compatibility and neutrality of the interface between a and c domains. In addition to the a/c twin domains, the simultaneous existence of different variants of a domains generates inevitably a/a 109°-type intersections.

In this article we address the intersection of a domains in GeTe thin films and explore the formation of nontrivial polarization configurations. Since a domains are already constrained by the interaction with the majority c domain that is in epitaxy with the Si substrate, the crossing of a domains generates major problems of mechanical and electrical compatibilities. We show that a huge structural lattice reorganization occurs and domain walls are formed. In particular the rhombohedron lattice angle decreases by 1°, the lattice rotates by more than 4° and a periodic network of charged domain

*frederic.leroy.3@univ-amu.fr

walls is formed perpendicular to the surface plane. These results, addressed by 3D reciprocal space maps and scanning tunneling microscopy, point to a complex polarization texture of GeTe thin films at a/a intersections while second-harmonic generation (SHG), supported by machine learning methods, reveals different crossing types and an unchanged symmetry at the intersection regions.

II. EXPERIMENTAL METHODS

Si(111) wafers (Siltronix; 550-μm thick; $\rho = 1 - 10\,\Omega$cm) are first cleaned by acetone and ethanol rinsing before introduction in ultrahigh vacuum (UHV, 10^{-8} Pa). Then the substrates are degassed at 1000 K during 12 h followed by repeated high temperature annealing (1500 K) during a few minutes in order to obtain a clean 7×7 surface reconstruction. First a deposition of one monolayer of Sb is performed on the Si(111) surface, forming the so-called Si(111)-$\sqrt{3} \times \sqrt{3}$-Sb reconstruction that greatly improves the crystalline quality of the GeTe film [23]. The GeTe thin films are grown by codeposition of Ge (1175 °C) and Te (310 °C) in UHV on a sample maintained at 275°C. In these conditions the flux ratio between Ge:Te is fixed at 2:5 in order to compensate for the high desorption rate of Te [25]. All the deposition sources are effusion cells from MBE-Komponenten Gmbh. After growth, the samples are transferred under UHV conditions thanks to a homemade transfer suitcase and characterized by scanning tunneling microscopy (STM) with a VT-STM (Scienta Omicron Gmbh). STM images were obtained at room temperature in constant current mode with typical imaging conditions (U =–1 V, I = 20 pA, W tip). The internal structure of thick GeTe films (>40 nm) has been studied by x-ray diffraction at BM32 beamline (ESRF). X-ray diffraction data have been measured at 18 keV [$\lambda = 0.06888$ nm] with a beam size of 200×300 μm^2 and collected onto a 2D detector. The data have been converted from the detector coordinates (pixel index) to diffraction angles and then to reciprocal space coordinates. To protect the GeTe surface from contamination during sample transfer to the ESRF UHV chamber, a Te capping was used. The capping is removed in UHV first by a mild Ar ion bombardment at room temperature (1 keV, 10 μA) to remove the topmost oxidized layers then by annealing at 220 °C to desorb the complete Te layer. Second-harmonic generation (SHG) microscopy and polarimetry measurements are conducted in an inverted optical microscope. The fundamental wave is provided by a laser source emitting pulses of 100-fs duration at a repetition rate of 80 MHz, centered at a wavelength $\lambda = 800$ nm. The sample is illuminated at normal incidence with a time-averaged power of about 10 mW. The SHG images are obtained by scanning the sample with respect to the focused laser beam (objective ×60, 0.85 numerical aperture) using computer-controlled stepping motors. The output intensity is spectrally filtered and collected into a photomultiplier. Polarimetry measurements are performed by recording the SHG images at different polarizer and analyzer angles (ϕ and α, respectively) [26]. The automatic polarimetry data analysis is supported by machine learning methods [27] for fast and efficient detection of the nanostrip domain crossing regions. The analysis workflow presented in this study is implemented using Python 3. The program allows us to load and preprocess the SHG data cube (stack of images recorded at different polarizer and analyzer configurations) and display the results. The K-means and non-negative matrix factorization (NMF) algorithms are implemented via open-access Python packages [28] and applied to the SHG polarimetry data for the automatic determination of the domain variants as detailed in Ref. [27].

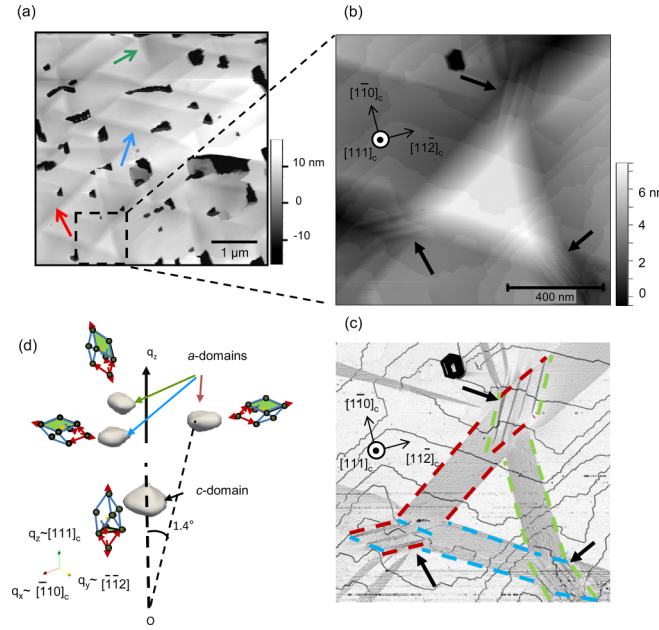

FIG. 1. (a) STM image of a 800-nm-thick GeTe thin film grown on Si(111)-$\sqrt{3} \times \sqrt{3}$-Sb (U =–1 V, I = 20 pA). The arrows show needle-shape a-type domains at the surface. The colors indicates the three variants of a domains. (b) Close view of three domains crossing showing the staircase morphology (black arrows). (c) Derivative of STM image (b) to highlight the morphological slopes at the surface corresponding to a domains surface and a/a crossings. (d) 3D reciprocal space map of 222_c, $22\bar{2}_c$ $\bar{2}\bar{2}2_c$, and $\bar{2}22_c$ GeTe Bragg peaks. q_x, q_y, and q_z are the reciprocal space coordinates that are aligned respectively along $[\bar{1}10]_c$, $[\bar{1}\bar{1}2]_c$, and $[111]_c$ directions. The main peak at (0, 0, 35.40 nm^{-1}) coordinate arises from the major c domain (rhombohedron axis perpendicular to surface) and the three other Bragg peaks, at higher q_z [(0,–0.96, 36.73 nm^{-1}), (–0.80, 0.46, 36.72 nm^{-1}) and (0.70, 0.50, 36.71 nm^{-1})], result from the three a domains with rhombohedron axis nearly in-plane. The surface planes of the a domains are tilted by 1.4° with respect to the Si(111) surface

III. RESULTS AND DISCUSSION

The surface morphology of a 800-nm-thick GeTe film grown on Si(111)-$\sqrt{3} \times \sqrt{3}$-Sb surface shows needle shape structures [Fig. 1(a)] crossing the surface over several microns in the $\langle 1\bar{1}0 \rangle_c$ directions. These needles are a few hundreds of nanometer wide and show a slightly tilted surface plane with respect to the main surface. These needles point out the presence of ferroelectric a domains whereas the flat layer is made of the c domain [24]. The corresponding 3D reciprocal space map around the symmetric Bragg peak of GeTe, perpendicular to the surface plane, shows indeed four contributions [see Fig. 1(d)]. The main one labeled 222_c, at low q_z, is due to the majority c domain with a rhombohedron axis of the

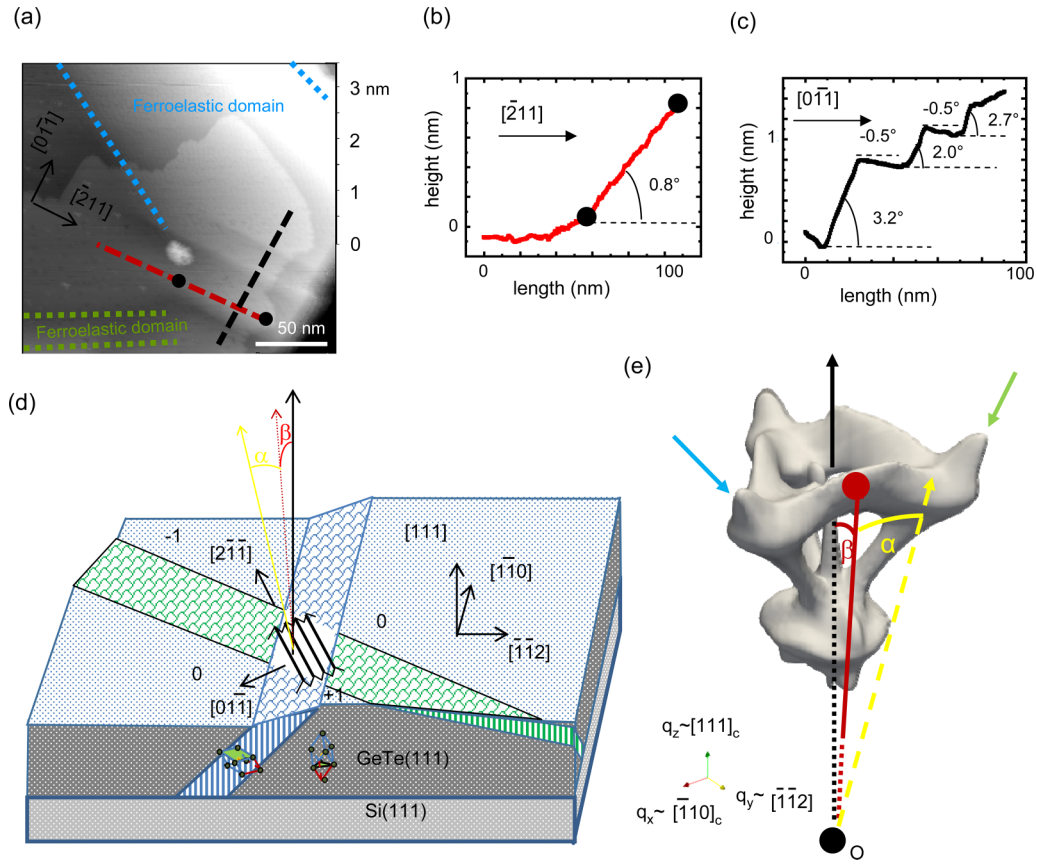

FIG. 2. (a) STM image of an intersection area of two *a* domains. (b) Line profile along the $[\bar{2}11]_c$ direction [along red dashed line in (a)] showing a slight tilt angle of the edge. (c) Line profile along the $[0\bar{1}1]_c$ direction [along dark dashed line in (a)] showing a staircase morphology of the surface. (d) Schematic view of the GeTe film, *c*- and *a*-type ferroelastic domains as well as a *a*/*a* intersection. The rhombohedron unit cell is given in the *c* domain and in a *a* domain. The two *a* domains extend as stripes elongated along $[10\bar{1}]_c$ and $[1\bar{1}0]_c$ directions. Their crossing forms a staircase morphology (black lines) along $[01\bar{1}]_c$ that is translation invariant along $[2\bar{1}\bar{1}]_c$ direction. α represents the tilt angle of the surface with respect to $[111]_c$ and oriented in $[01\bar{1}]_c$ direction. β represents the tilt angle of the surface with respect to $[111]_c$ and oriented in $[2\bar{1}\bar{1}]_c$ direction. (e) 3D reciprocal space maps around 222_c, $22\bar{2}_c$ $2\bar{2}2_c$, and $\bar{2}22_c$ GeTe Bragg peaks: the x-ray scattered intensity arising from the intersections is expected to be in-between two Bragg peaks. The corresponding diffuse scattering is tilted by an angle β with respect to the c axis in the $[\bar{1}\bar{1}2]_c$ direction and the staircase morphology generates a diffuse arc tilted by an angle α in the $[\bar{1}10]_c$ direction.

unit cell normal to the surface. The three other Bragg peaks $22\bar{2}_c$, $2\bar{2}2_c$, and $\bar{2}22_c$ at higher q_z and slightly off the specular rod by 1.4°, are due to three *a* domains variants with axes of the rhombohedron unit cell tilted by ∼71° with respect to the normal to the surface. As can be seen on Fig. 1(a), the density of *a* domains in thick GeTe films is such that crossing of *a* domains frequently occurs. Figure 1(b) shows a close view of the GeTe surface by STM. The derivative of the surface morphology highlights specific surface structures [Fig. 1(c)]. The thinnest dark lines correspond to atomic steps. The *a* domains appear as needles with a grey contrast due to the tilt angle of the surface plane. Their typical width is 100–200 nm. In this region all three variants of *a* domains exist and when two *a* domains intersect they form a staircase surface morphology with a typical period of 30 − 50 nm along the $\langle 1\bar{1}0\rangle_c$ direction [see Figs. 1(b) and 1(c)]. The morphology of the intersection is translation invariant along the $\langle 11\bar{2}\rangle_c$ direction, i.e., along the bisector of the intersecting *a* domains. This local change of surface morphology claims for a change of domain walls.

To address these changes we have characterized the surface topography by STM in combination with 3D reciprocal space map analysis. The height profile of the intersecting area along the translation-invariant $[\bar{2}11]_c$ direction shows a small angle of $0.8° \pm 0.1°$ of the surface plane with respect to the flat *c* domain [Fig. 2(b)]. This angle corresponds to the angle of the intersecting line of two tilted surface planes of two *a* domains with respect to the *c*-domain surface $[1.4° \times \cos(60°) = 0.7°]$. In reciprocal space such a tilted surface should give a contribution in-between the Bragg peaks of two *a* domains. Indeed by reducing the iso-intensity surface of the 3D reciprocal space map around *a*-domain Bragg peaks, we observe some diffuse scattering at this reciprocal space coordinate [Fig. 2(e)]. Even more, the 3D reciprocal space map shows an arc of diffuse scattering that connects each Bragg peak of *a* domains. This signal suggests a strong interaction between intersecting *a* domains that can be assigned to a lattice relaxation process. In particular the diffuse scattering arc suggests not only a mean lattice rotation towards the $\langle\bar{1}\bar{1}2\rangle_c$ direction by $\beta = 0.8°$ but also towards the $\langle\bar{1}10\rangle_c$ direction [angle α, see Figs. 2(d) and 2(e)]. Indeed the STM height profile of the staircase morphology shows large slope variations of the surface that should give x-ray diffuse

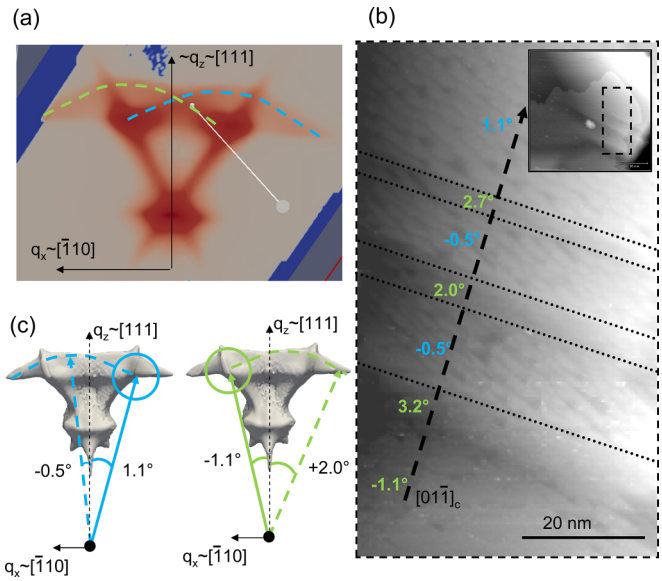

FIG. 3. (a) Cross section of the 3D reciprocal space map passing through the Bragg peaks of two a domains. Evidence of two crossing diffuse tails are highlighted by dashed lines. (b) Close STM view of the surface reconstruction of intersecting domains Inset: Large view of the surface and corresponding imaged area. The dashed lines separate the areas with specific surface reconstructions and thus identify different a-domain type. The indicated surface angles along $[01\bar{1}]_c$ direction are indicated in blue or green depending on the a domain [values extracted from the height profile of Fig. 2(c)]. (c) 3D reciprocal space maps and schematic representation of the corresponding expected x-ray scattered intensity from typical measured surface tilt angles by STM.

scattering contributions along the connecting arc [Fig. 2(c)]. Let us note that the x-ray diffraction measurement provides a continuous arc since it is based on a macroscopic sampling of the lattice relaxations at domain intersections whereas STM images provide a local characterization with a few measured tilt angles corresponding to a local relaxation state. To be complete, let us note that Fig. 2(e) shows also diffuse scattering rods connecting a and c domains Bragg peaks. As shown by Croes *et al.* [24] this diffuse scattering originates from the facetted interface associated with a/c domain walls (71°-type domain wall). The domain walls generate diffuse scattering rods, called crystal truncation rods for surfaces, starting on each Bragg peaks of the corresponding a and c domains and extending perpendicular to the domain wall, forming the measured diffuse scattering tails.

The vertical cross section of the 3D reciprocal space map passing through two Bragg peaks of a-type domains using a lower iso-intensity value brings additional information on the crossings [see Fig. 3(a)]. It shows that the diffuse scattering arc is not simply connecting the two Bragg reflections. It is in fact composed of two diffuse tails that start at each Bragg peak and extend towards the neighboring Bragg peak, passing slightly above and continuing even further away forming an arc of a circle (green and blue dashed lines). This surprising result shows that huge rotations of the GeTe lattice occur in the intersection zone. As the diffuse tail from one Bragg peak extends to the neighboring Bragg peak (and vice versa), then we can say that the surface planes of two intersecting a domains rotate so much that they appear to exchange their surface tilt angles in the crossing area. As this diffuse scattering is measured even further away from the neighboring Bragg peak, this indicates that the surface angle of one a domain can be more tilted than the neighboring a domain (away from the intersection area). This x-ray diffraction result is corroborated by high-resolution STM images. A close view of the intersecting area of two a domains shows the details of the surface structure [Fig. 3(b)]. As shown by Croes and coworkers [29], the surface termination of a domains displays surface reconstructions with large unit cells designed as row and scale structures. One can observe in the intersection area that the slope change of the staircase morphology is associated with a change of orientation of the surface reconstruction. If we associate the surface reconstruction with each a domain we observe that the surface normal of a a domain alone (without intersection) is tilted by $\alpha = -1.1°$ in the $[01\bar{1}]_c$ direction as expected from mechanical compatibility with the c domain [$-1.2° = -1.4° \times \cos(30°)$] whereas it is tilted by $\alpha = +3.2°$, $+2.0°$, and $+2.7°$ in the a/a intersection area. Similarly the other a domain is tilted by $\alpha = +1.1°$ in the $[01\bar{1}]_c$ direction as expected from mechanical compatibility with the c domain but tilted by $-0.5°$ in the intersection area. In Fig. 3(c) are schematically shown the expected positions of the x-ray scattering signal on the 3D-reciprocal space map assuming similar lattice rotations. They perfectly fit on the diffuse scattering arc.

To interpret this result let us study the mechanical compatibility conditions of two intersecting a domains. At first, i.e., away from a/a intersection, both a domains form 71°-type domain walls with the majority c domain [24]. Assuming that the c domain keeps a planar interface with the Si(111) substrate then the $(111)_c$ surface planes of a domains are expected to be tilted by 1.39° as deduced from the rhombohedral angle (58.3°) of GeTe and mechanical compatibility conditions at 71°-type domain walls. This is indeed confirmed by STM observations and x-ray diffraction (∼1.4°). The theoretical 1.39° tilt angle [24] can be decomposed in a rotation of the lattice (2.08°) and a pure shear component (−0.69°). This geometrical result is schematically illustrated in Figs. 4(a) and 4(b) showing the tilt angles of $(111)_c$ surface planes of two a domains with rhombohedron axes along $[11\bar{1}]_c$ and $[\bar{1}11]_c$ (the coordinates refer to the c domains pseudocube). However, in the intersection area, a staircase morphology is observed. This indicates a local rearrangement of polarization and the existence of additional domain patterns separated by domain walls. From the symmetry properties of rhombohedral GeTe and translation invariance of the staircase morphology along $\langle 11\bar{2}\rangle_c$ we can estimate that a/a domain walls are $(\bar{1}01)_c$ crystallographic planes forming 109°-type domain wall that are perpendicular to the $(111)_c$ surface plane. Such domain walls necessitate a reorganization of the crystal lattice to minimize the interfacial strain field at a/a crossing. In particular one can quantify the necessary rotation to ensure mechanical compatibility at such an interface. Figure 4(c) shows a schematic representation of the tilt angles of $(\bar{1}01)_c$ crystallographic plane of two a domains with rhombohedron axes along $[11\bar{1}]_c$ and $[\bar{1}11]_c$. In absence of intersection, the $(\bar{1}01)_c$ crystallographic planes of two a domains are tilted

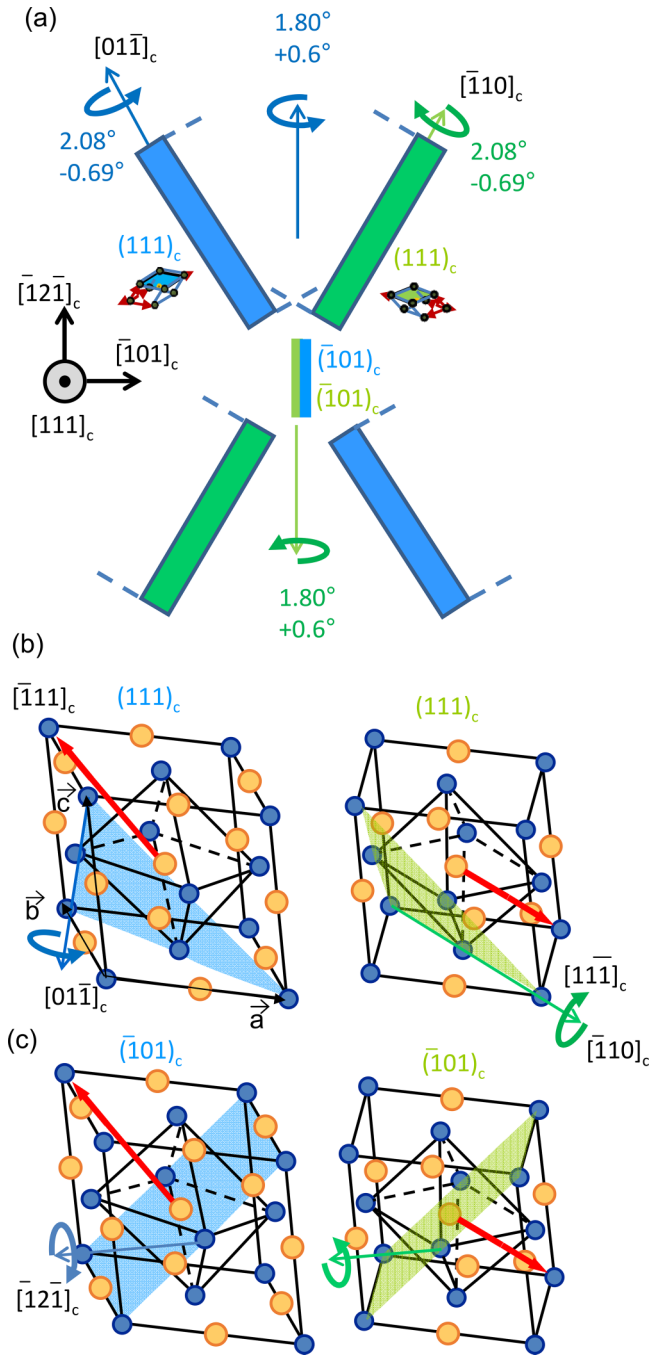

FIG. 4. (a) Schematic representation of two intersecting a domains. Considering pseudocubic unit cells, the $(111)_c$ surface planes and the $(\bar{1}01)_c$ domain wall planes are represented with their rotations (without intersection). The $(111)_c$ surface plane of a domains is expected to be tilted by $2.08° - 0.69° = 1.39°$ with respect to Si(111) surface (2.08° from lattice rotation and −0.69° from shear). The $(\bar{1}01)_c$ domain wall plane of a domains is expected to be tilted by $1.80° + 0.60° = 2.40°$ with respect to Si$(\bar{1}01)_c$ plane (1.80° from lattice rotation and +0.60° from shear. (b) Same as (a) but representing the pseudocubic unit cells for two a domains elongated along $[\bar{1}11]_c$ and $[11\bar{1}]_c$. The filled areas (blue and green) represent the $(111)_c$ surface plane that tilts due to the stretching of the rhombohedron. (c) Same as (b) but considering the tilt of the $(\bar{1}01)_c$ plane corresponding to the domain wall generated by the a/a intersection.

with respect to the $[\bar{1}2\bar{1}]$ axis in opposed directions by +2.4° and −2.4° [1.8° arises from the rotation imposed by the a/c mechanical compatibility and +0.60° from pure shear, see Fig. 4(a)]. To force the two crystal lattices to mechanically match in the same $(\bar{1}01)_c$ plane, a rotation of the crystals towards each other by $2.4 \times 2 = 4.8°$ is necessary. In this circumstance either both domains rotate simultaneously or alternatively. STM image of Fig. 3(b) shows that both domains rotate alternatively and form a staircase surface morphology. The smallest domain (width) at the intersection undergoes the largest rotation. For instance, outside the intersection area, the surface plane of the smallest a domain in Fig. 3(b) is tilted by $\alpha = -1.1°$ and in the intersecting area, it can rotate around the $[\bar{1}2\bar{1}]_c$ axis by +4.3° to reach $\alpha = +3.2°$ at maximum. The largest a domain rotates less (−1.6°), from $\alpha = +1.1°$ outside the intersecting area to $\alpha = -0.5°$ inside. From these measurements we observe that the rotations of the a domains in the intersection areas are extremely large but not enough to achieve a complete lattice relaxation at the domain wall (4.8°). This points to a residual stress due to the additional mechanical contributions related to the interface with the c domains and to the epitaxy with the Si substrate. In addition let us note that the observed rotation of the lattices to adjust the $(\bar{1}01)_c$ domain wall of two intersecting a domains should not occur only around the $[\bar{1}2\bar{1}]_c$ axis. The $(\bar{1}01)$ plane is also expected to rotate by 0.85° around the surface normal in opposed directions for both a domains to be mechanically compatible. This rotation is, however, much smaller than around the $[\bar{1}2\bar{1}]_c$ axis and the generated mechanical stress does not induce a deep restructuring of the lattices.

Apart from the lattice rotation a close inspection of the reciprocal space coordinates of the diffuse x-ray scattering tails around the Bragg peaks of a domains show that the intereticular distances are also modified at the intersections. To quantify the induced structural changes we have measured 3D reciprocal space maps around different Bragg peaks. In Fig. 5(a) is shown a 3D map of GeTe thin film including the 222_c Bragg peak and also the nonsymmetric $\bar{2}22_c$ Bragg peak (considering as reference for reciprocal space coordinates the c domains). The $\bar{2}22_c$ Bragg peak is angularly distant by ∼71° with respect to the normal to the surface. It probes the intereticular distance along the rhombohedron axis of one variant of a domain. As for a-domains Bragg peaks around the 222_c, the Bragg peaks of the a domains around $\bar{2}22_c$ Bragg reflection shows diffuse scattering tails that can be assigned to lattice relaxations. In particular a diffuse tail starting from the Bragg peak of the a domain that is stretched along the probed axis, i.e., the rhombohedron axis, extends far away [see Fig. 5(b)(i)]. This tail can be assigned to a rotation of the lattice around $[\bar{1}\bar{1}2]_c$ direction as for the 222_c diffuse tail. In Figs. 5(b)(ii) and 5(c)(ii) are represented the evolution of the modulus of the scattering vectors as function of the lattice rotation angle α following the diffuse scattering tails for 222_c and $\bar{2}22_c$ Bragg peaks. For the 222_c diffuse tail, the modulus of the scattering vector increases from 36.6 nm^{-1} and reaches a maximum at 37.2 nm^{-1} (+1.6%) for $\alpha \sim 2°$ and then decreases at larger angle. Similarly the modulus of the scattering vector of the $\bar{2}22_c$ diffuse tail decreases from 35.3 to 34.9 nm^{-1} (−1.1%) for $\alpha \sim 2°$ and then increases again

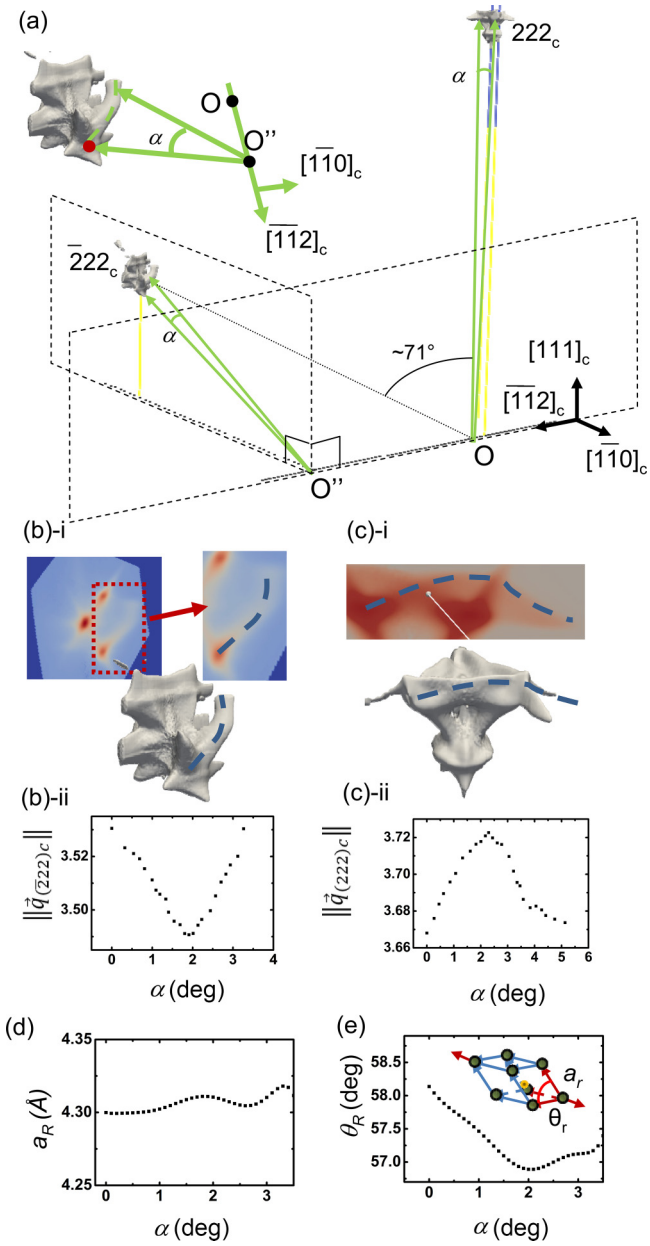

FIG. 5. (a) Complete 3D reciprocal space maps around $\bar{2}22_c$ and 222_c Bragg peaks (c domain is selected as the reference domain for reciprocal space coordinates). (b)(i) Close view of the 3D reciprocal space map around $\bar{2}22_c$. The dashed line illustrates the position of the diffuse tail starting from the a-domain Bragg peak. (b)(ii) Evolution of the modulus of the scattering vector along the diffuse tail as function of the rotation angle α. (c) Same as (b) for the 222_c Bragg peak. (d) Plot of the rhombohedron lattice parameter at the intersection as function of rotation angle α. (e) Plot of the rhombohedron angle at the intersection as function of rotation angle α.

at larger angle. The decrease of the modulus of the scattering vector of the $\bar{2}22_c$ diffuse tail clearly indicates an extension of the intereticular distance along the rhombohedron axis of the a domain. This result is also corroborated by the decrease of the intereticular distance deduced from 222_c diffuse tail position. This set of data can be combined to determine the change of structure of the GeTe lattice in the intersection area. We could not detect a change of symmetry and the rhombohedral structure appears to be present even in the intersection area. Outside the intersections, from the Bragg peak positions, we obtain a rhombohedron lattice parameter $a_R = 0.430$ nm and angle $\theta_R = 58.2°$. In the intersection area ($\alpha \sim 2°$) we obtain a slight increase of the lattice parameter ($a_R = 0.431 - 0.432$ nm) and a large decrease of the rhombohedron angle $\theta_R = 57.0°$. Such a large structural modification is expected to result in a large change of ferroelectric polarization of the material.

Second-harmonic generation microscopy (SHG) with polarimetry analysis is used to examine and compare the local symmetry at the strip-domain (staircase) intersections with respect to that of the parent material to detect a possible phase change at the intersections. The intersection regions are first detected using the K-means method applied to the SHG images recorded at different polarizer and analyzer angle settings, following the method reported in [27,30] and in the Supplemental Material [22]. While the K-means clustering method allows the determination of the domain variants and infers the position of their intersections, it restricts the assignment of the data points to only one cluster. To disentangle the mixed signals from the main c domain (background) and the three different a domains (nanostrips) in GeTe, especially at the a-domain intersections, we use the non-negative matrix factorization (NMF) algorithm on the SHG polarimetry data [27]. Because of the small size of the crossings (about 50 nm) and the long acquisition time due to the slow sample scanning with respect to the laser in nonlinear optical microscopy, the SHG study contains a rather limited number of data points. To increase the accuracy of the data analysis, we trained the machine learning models on a larger data set, including the data reported in [24,27] (see supplementary materials for details in [22]). Figure 6 summarizes the different types of nanostrip crossings as automatically derived from the SHG polarimetry analysis using trained machine learning methods. Each SHG polarimetry plot associated with each pixel of the GeTe film can be decomposed in four components with distinct polar plots corresponding to the contributions from the c domain (black background) and the three a domains variants (RGB colors). All detected crossing regions contain the signatures of the two a domains forming the intersection. The intersection of strip domains can result in either uninterrupted or interrupted stripes, or a rearrangement of one of the intersecting strip domains (e.g., splitting into two parts after crossing another a domain). However, it is worth noting that the interrupted configuration (one of the strip domains is stopped at the intersection region) is most commonly observed and occurs systematically in thin films with thicknesses below 400 nm. Decomposing the data into more than four polar plots does not provide relevant polar plots (see Supplemental Material and Fig. 8 in [22]), showing that the intersections do not contain an additional phase. The absence of symmetry variation in the SHG study confirms that the a domains at the intersections are rhombohedral.

The remaining question concerns the charge state of the $(\bar{1}01)_c$ 109°-type domain walls formed at these a/a domain intersections. Figure 7(a) is a schematic view of the polarization state of the c domain and of two needle shape a domains. Since the polarization state of the c domain is along

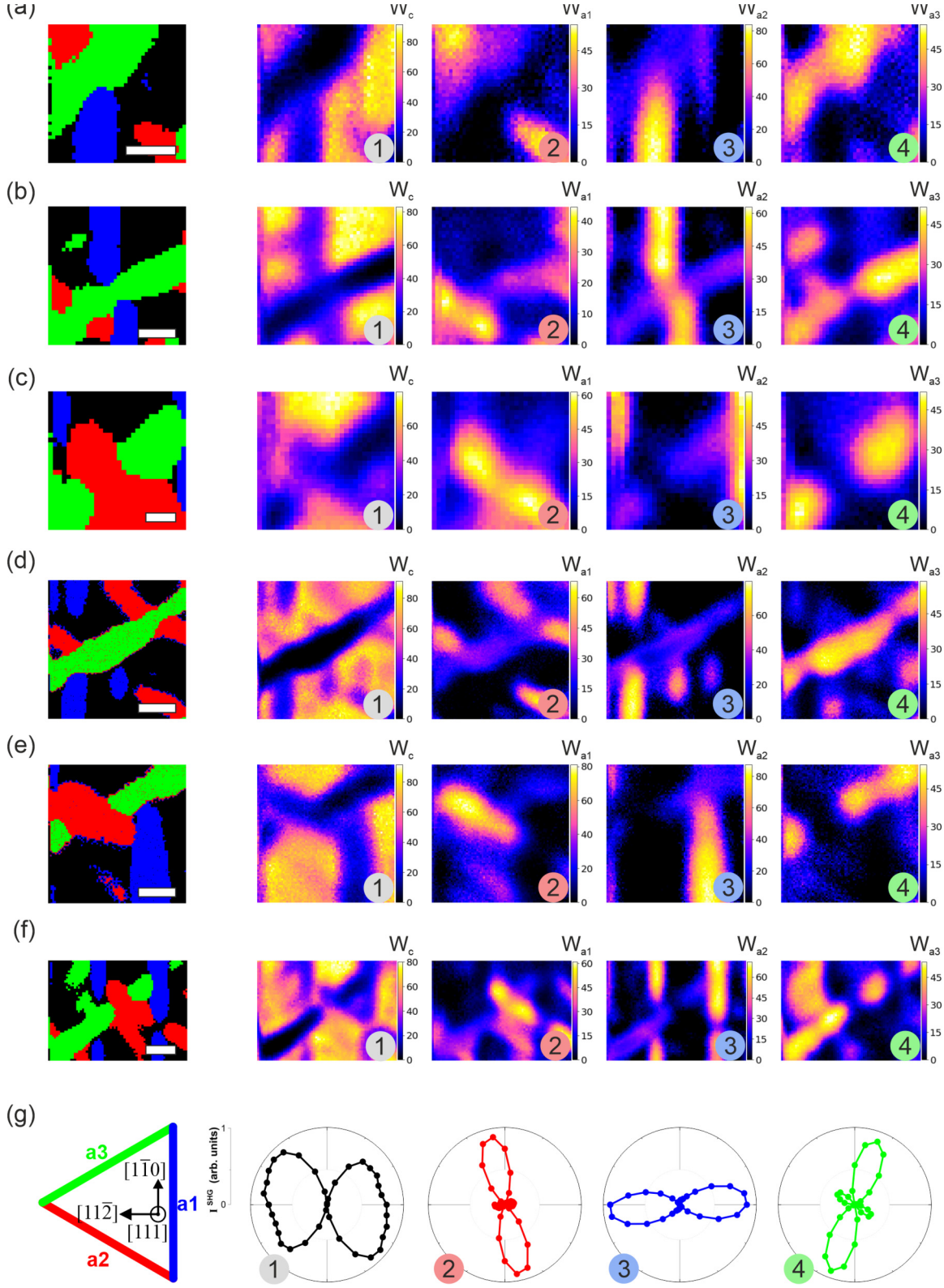

FIG. 6. Local [(a)–(f)] different strip domain intersection types derived from SHG microscopy polarimetry analysis assisted by trained K-means (left columns) and NMF algorithms at *a* domains intersections. The domain contribution maps derived with NMF are obtained by taking into account four components (domain variants) with respective fractions W_i corresponding to the polar plots presented in panel (g). The scale bar is common to all images and corresponds to 1 μm.

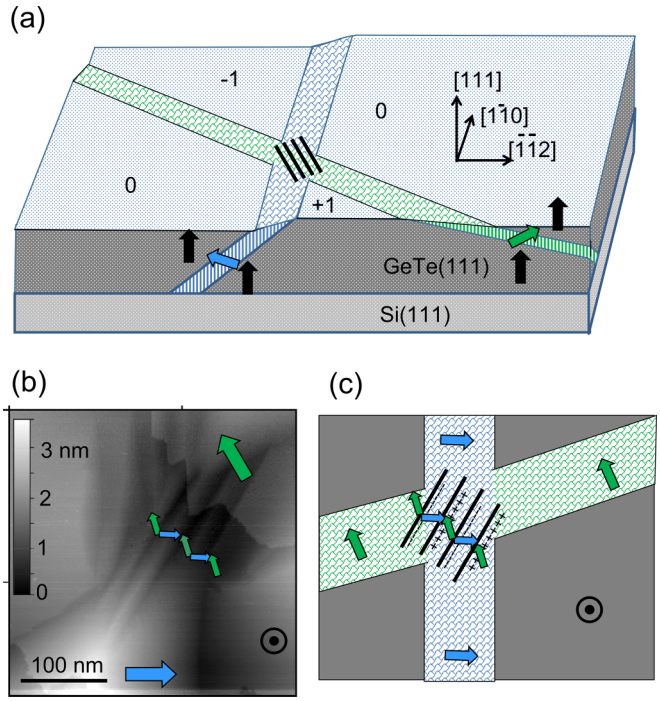

FIG. 7. (a) Model of the surface morphology and polarization states of *a* domains and *c* domain. (b) STM image of the surface topography of an intersecting area of two *a* domains. The arrows show the in-plane components of the polarization direction at different places. (c) Corresponding schematic representation of the staircase morphology indicating the presence of charged domain walls.

$[111]_c$, pointing upward [18], then to have a neutral 71°-type domain wall, the polarization state of the *a* domains is expected to be along $[11\bar{1}]_c$ and $[1\bar{1}1]_c$. Therefore the formation of $(\bar{1}01)_c$ domain walls at a/a intersections results in noncompensated charges. The staircase morphology observed by STM [Fig. 7(b)] with alternate *a* domains results in head-to-head and tail-to-tail polarization configurations at domain walls [Fig. 7(c)]. The formation of charged domain walls in GeTe thin films seems to be driven by mechanical compatibility, the electrostatic part being compensated by the available charges in the materials [31–33]. As proposed by Dangic and co-workers [7], charged domain walls are expected to be easily formed in GeTe. Indeed GeTe can provide free charge carriers to locally screen the accumulated charges since it is semiconducting and p doped (due to the easy formation of Ge vacancies [34]). The positively charged carriers may compensate the accumulated charge at tail-to-tail domain walls whereas the corresponding Ge vacancies (negatively charged) could accumulate at head-to-head domain walls if they are enough mobile [35]. Since screening by free charge carriers is expected to be much faster than by ions, the conductivity at tail-to-tail domain walls should be higher than at head-to-head domain walls in GeTe.

IV. CONCLUSIONS

In conclusion we have studied the *a* domain intersections in ferroelectric GeTe thin films grown on Si(111)-Sb. Constrained by the mechanical compatibility conditions between *a* and *c* domains as well as by the epitaxy of the thin film with the silicon substrate, the a/a domain intersections are *a priori* highly mismatched. To minimize the energy cost of these intersections, a complex structural reorganization occurs as demonstrated by 3D reciprocal space maps, scanning tunneling microscopy, and second-harmonic generation. We demonstrate the formation of domain walls, large lattice rotations, enhanced stretching of the rhombohedral lattice of GeTe. We believe that the detailed description of a/a domain intersections and 109°-type domain wall will motivate further studies for the control of the ferroelectric polarization texture in GeTe thin films.

ACKNOWLEDGMENTS

The project leading to this publication has received funding from Excellence Initiative of Aix-Marseille University A*MIDEX, a french "Investissements d'Avenir" programme through the AMUtech Institute. This work has also been supported by the ANR Grant FETh (ANR-22-CE08-0023). B.C. and S.C.-H. acknowledge the Interdisciplinary Thematic Institute EUR QMat (ANR-17-EURE-0024), as part of the ITI 2021-2028 Program supported by the IdEx Unistra (ANR-10-IDEX-0002) and SFRI STRAT'US (ANR-20-SFRI-0012) through the French Programme d'Investissement d'Avenir. We deeply thank Lucio Martinelli for x-ray measurements (Synchrotron ESRF, BM32, Grenoble, France).

[1] A. Gruverman, D. Wu, H.-J. Fan, I. Vrejoiu, M. Alexe, R. J. Harrison, and J. F. Scott, Vortex ferroelectric domains, J. Phys.: Condens. Matter **20**, 342201 (2008).

[2] N. Balke, B. Winchester, W. Ren, Y. H. Chu, A. N. Morozovska, E. A. Eliseev, M. Huijben, R. K. Vasudevan, P. Maksymovych, J. Britson *et al.*, Enhanced electric conductivity at ferroelectric vortex cores in $BiFeO_3$, Nat. Phys. **8**, 81 (2012).

[3] Y. L. Tang, Y. L. Zhu, X. L. Ma, A. Y. Borisevich, A. N. Morozovska, E. A. Eliseev, W. Y. Wang, Y. J. Wang, Y. B. Xu, Z. D. Zhang, and S. J. Pennycook, Observation of a periodic array of flux-closure quadrants in strained ferroelectric $PbTiO_3$ films, Science **348**, 547 (2015).

[4] A. K. Yadav, C. T. Nelson, S. L. Hsu, Z. Hong, J. D. Clarkson, C. M. Schlepueetz, A. R. Damodaran, P. Shafer, E. Arenholz, L. R. Dedon *et al.*, Observation of polar vortices in oxide superlattices, Nature (London) **530**, 198 (2016).

[5] P. Shafer, P. Garcia-Fernandez, P. Aguado-Puente, A. R. Damodaran, A. K. Yadav, C. T. Nelson, S.-L. Hsu, J. C. Wojdel, J. Iniguez, L. W. Martin *et al.*, Emergent chirality in the electric polarization texture of titanate superlattices, Proc. Natl. Acad. Sci. USA **115**, 915 (2018).

[6] S. Das, Y. L. Tang, Z. Hong, M. A. P. Goncalves, M. R. McCarter, C. Klewe, K. X. Nguyen, F. Gomez-Ortiz, P. Shafer, E. Arenholz *et al.*Observation of room-temperature polar skyrmions, Nature (London) **568**, 368 (2019).

[7] D. Dangic, E. D. Murray, S. Fahy, and I. Savic, Structural and thermal transport properties of ferroelectric domain walls in GeTe from first principles, Phys. Rev. B **101**, 184110 (2020).

[8] D. Dangic, S. Fahy, and I. Savic, Giant thermoelectric power factor in charged ferroelectric domain walls of GeTe with Van Hove singularities, npj Comput. Mater. **6**, 195 (2020).
[9] M. Hong and J. Zou, and Z.-G. Chen, Thermoelectric GeTe with diverse degrees of freedom having secured superhigh performance, Adv. Mater. **31**, 1807071 (2019).
[10] S. Roychowdhury, M. Samanta, S. Perumal, and K. Biswas, Germanium chalcogenide thermoelectrics: Electronic structure modulation and low lattice thermal conductivity, Chem. Mater. **30**, 5799 (2018).
[11] S. Perumal, S. Roychowdhury, and K. Biswas, High performance thermoelectric materials and devices based on GeTe, J. Mater. Chem. C **4**, 7520 (2016).
[12] J. Li, X. Zhang, S. Lin, Z. Chen, and Y. Pei, Realizing the high thermoelectric performance of GeTe by Sb-doping and Se-alloying, Chem. Mater. **29**, 605 (2017).
[13] E. M. Levin, M. F. Besser, and R. Hanus, Electronic and thermal transport in GeTe: A versatile base for thermoelectric materials, J. Appl. Phys. **114**, 083713 (2013).
[14] W.-D. Liu, D.-Z. Wang, Q. Liu, W. Zhou, Z. Shao, and Z.-G. Chen, High-performance GeTe-based thermoelectrics: From materials to devices, Adv. Energy Mater. **10**, 2000367 (2020).
[15] X. Zhang, Z. Bu, S. Lin, Z. Chen, W. Li, and Y. Pei, GeTe thermoelectrics, Joule **4**, 986 (2020).
[16] D. Di Sante, P. Barone, R. Bertacco, and S. Picozzi, Electric control of the giant Rashba effect in bulk GeTe, Adv. Mater. **25**, 509 (2013).
[17] A. V. Kolobov, D. J. Kim, A. Giussani, P. Fons, J. Tominaga, R. Calarco, and A. Gruverman, Ferroelectric switching in epitaxial GeTe films, APL Mater. **2**, 066101 (2014).
[18] C. Rinaldi, S. Varotto, M. Asa, J. Slawinska, J. Fujii, G. Vinai, S. Cecchi, D. Di Sante, R. Calarco, I. Vobornik, G. Panaccione, S. Picozzi, and R. Bertacco, Ferroelectric control of the spin texture in GeTe, Nano Lett. **18**, 2751 (2018).
[19] J. Krempasky, S. Muff, J. Minar, N. Pilet, M. Fanciulli, A. P. Weber, E. B. Guedes, M. Caputo, E. Mueller, V. V. Volobuev, M. Gmitra, C. A. F. Vaz, V. Scagnoli, G. Springholz, and J. H. Dil, Operando imaging of all-electric spin texture manipulation in ferroelectric and multiferroic Rashba semiconductors, Phys. Rev. X **8**, 021067 (2018).
[20] Y. Li, Y. Li, P. Li, B. Fang, X. Yang, Y. Wen, D.-X. Zheng, C.-H. Zhang, X. He, A. Manchon, Z.-H. Cheng, and X.-X. Zhang, Nonreciprocal charge transport up to room temperature in bulk Rashba semiconductor alpha-GeTe, Nat. Commun. **12**, 540 (2021).
[21] S. Varotto, L. Nessi, S. Cecchi, J. Slawinska, P. Noel, S. Petro, F. Fagiani, A. Novati, M. Cantoni, D. Petti *et al.*, Room-temperature ferroelectric switching of spin-to-charge conversion in germanium telluride, Nat. Electron. **4**, 740 (2021).
[22] See Supplemental Material at http://link.aps.org/supplemental/10.1103/PhysRevB.109.024103 for relationship between the rhombohedral and the pseudocubic unit cells and detailed methodology for the determination of ferroelectric domains structure measured by SHG.
[23] R. Wang, J. E. Boschker, E. Bruyer, D. Di Sante, S. Picozzi, K. Perumal, A. Giussani, H. Riechert, and R. Calarco, Toward truly single crystalline GeTe films: The relevance of the substrate surface, J. Phys. Chem. C **118**, 29724 (2014).
[24] B. Croes, F. Cheynis, Y. Zhang, C. Voulot, K. D. Dorkenoo, S. Cherifi-Hertel, C. Mocuta, M. Texier, T. Cornelius, O. Thomas, M.-I. Richard, P. Müller, S. Curiotto, and F. Leroy, Ferroelectric nanodomains in epitaxial GeTe thin films, Phys. Rev. Mater. **5**, 124415 (2021).
[25] K. Perumal, Epitaxial growth of Ge-Sb-Te based phase change materials, PhD. thesis, Humboldt-Universität zu Berlin, Mathematisch-Naturwissenschaftliche Fakultät I (2013).
[26] S. Cherifi-Hertel, C. Voulot, U. Acevedo-Salas, Y. Zhang, O. Grégut, K. D. Dorkenoo, R. Hertel, Shedding light on non-Ising polar domain walls: Insight from second harmonic generation microscopy and polarimetry analysis, J. Appl. Phys. **129**, 081101 (2021).
[27] B. Croes, I. Gaponenko, C. Voulot, O. Grégut, K. D. Dorkenoo, F. Cheynis, S. Curiotto, P. Müller, F. Leroy, K. Cordero-Edwards *et al.*, Automatic ferroelectric domain pattern recognition based on the analysis of localized nonlinear optical responses assisted by machine learning, Adv. Phys. Res. **2**, 2200037 (2023).
[28] F. Pedregosa, G. Varoquaux, A. Gramfort, V. Michel, B. Thirion, O. Grisel, M. Blondel, P. Prettenhofer, R. Weiss, V. Dubourg *et al.*, Scikit-learn: Machine learning in Python, J. Machine Learn. Res. **12**, 2825 (2011).
[29] B. Croes, F. Cheynis, P. Müller, S. Curiotto, and F. Leroy, Polar surface of ferroelectric nanodomains in GeTe thin films, Phys. Rev. Mater. **6**, 064407 (2022).
[30] I. Gaponenko, S. Cherifi-Hertel, U. Acevedo-Salas, N. Bassiri-Gharb, and P. Paruch, Correlative imaging of ferroelectric domain walls, Sci. Rep. **12**, 165 (2022).
[31] A. Crassous, T. Sluka, A. K. Tagantsev, and N. Setter, Polarization charge as a reconfigurable quasi-dopant in ferroelectric thin films, Nat. Nanotechnol. **10**, 614 (2015).
[32] T. Sluka, P. Bednyakov, A. K. Tagantsev, and N. Setter, Free-electron gas at charged domain walls in insulating $BaTiO_3$, Nat. Commun. **4**, 1808 (2013).
[33] P. S. Bednyakov, T. Sluka, A. K. Tagantsev, D. Damjanovic, and N. Setter, Formation of charged ferroelectric domain walls with controlled periodicity, Sci. Rep. **5**, 15819 (2015).
[34] V. L. Deringer, M. Lumeij, and R. Dronskowski, *Ab initio* modeling of alpha-GeTe(111) surfaces, J. Phys. Chem. C **116**, 15801 (2012).
[35] V. L. Deringer, M. Lumeij, R. P. Stoffel, and R. Dronskowski, Mechanisms of atomic motion through crystalline GeTe, Chem. Mater. **25**, 2220 (2013).